

Visualizing light trapping within textured silicon solar cells



Cite as: J. Appl. Phys. 127, 063104 (2020); doi: 10.1063/1.5131173

Submitted: 9 October 2019 · Accepted: 6 January 2020 ·

Published Online: 12 February 2020



Salman Manzoor,¹  Miha Filipič,² Arthur Onno,¹  Marko Topič,²  and Zachary C. Holman^{1,a)} 

AFFILIATIONS

¹School of Electrical, Computer and Energy Engineering, Arizona State University, Tempe, Arizona 85287, USA

²Faculty of Electrical Engineering, University of Ljubljana, Tržaška 25, SI-1000 Ljubljana, Slovenia

^{a)}Author to whom correspondence should be addressed: zachary.holman@asu.edu

ABSTRACT

Random pyramids are the most widely used texture in commercial monocrystalline silicon solar cells to trap weakly absorbed photons with near-bandgap energies. There has been steady improvement in efforts to model the light-trapping performance of random pyramids, including a shift from an assumed pyramid base angle of 54.7° (ideal-random pyramids) to smaller values that are consistent with measured average angles. However, simulations have not yet considered the effects of a distribution of base angles (real-random pyramids), which all real textured wafers have. In this contribution, we benchmark the light-trapping capability of real-random pyramids against ideal-random pyramids and Lambertian scatterers by performing ray tracing of an accurate three-dimensional topographical map of the surface of a textured silicon wafer measured using atomic force microscopy. The angular distribution function (ADF) of light rays within the wafer, calculated at each pass as rays bounce between the front and rear surfaces, reveals that real-random pyramids are superior to ideal-random pyramids in trapping light precisely because of the distribution in their base angle. In particular, the ADF inside a wafer with real-random pyramids evolves to be Lambertian within just two passes—by the time (non-absorbed) light re-arrives at the front surface. Furthermore, the total path-length enhancement of light reaches nearly 60—exceeding that of a wafer with Lambertian surfaces—for narrow angles of incidence, though it falls short of the Lambertian reference for oblique angles.

Published under license by AIP Publishing. <https://doi.org/10.1063/1.5131173>

I. INTRODUCTION

Commercial silicon solar cells have textures on their front and rear surfaces to minimize front-surface reflection and maximize the path length of weakly absorbed light. The former is routinely measured and used to tune the texturing process, but the latter is difficult to quantify experimentally because the relevant measurable quantity—the total absorbance—conflates light trapping with parasitic absorption. (Throughout this paper, “light trapping” refers exclusively to the path length in the absence of absorption and, thus, depends only on texture and refractive index; “parasitic absorption” refers to absorption in layers other than the wafer.) To disentangle these processes and understand how a given texture traps light, it is common to simulate, at sub-bandgap wavelengths, representative silicon solar cell structures with perfect front transmission and rear reflection, like that shown in Fig. 1.

Monocrystalline silicon solar cells are fabricated on (100) wafers that are textured in alkaline solutions, leading to anisotropic etching of the front and rear surfaces. The resulting pyramids have

random positions and heights but not, ideally, random base angle (α_B). The expected base angle is 54.7° and is defined by the angle between the (111) and (100) planes. Randomly distributed pyramids with this ideal base angle are referred to as “ideal-random” in this paper. Previous optical simulations have studied light trapping in wafers with ideal-random pyramids using ray tracing and compared the path-length enhancement (PLE) to that achieved with other textures.^{1–8} The benchmark in these comparisons is usually Lambertian (i.e., isotropic scattering) surfaces, which provide an average path-length enhancement (i.e., averaged over all possible ray paths) of $4n^2$ for weakly absorbed light, with n being the refractive index of the absorbing material.⁹ Lambertian surfaces are only one particular light-trapping scheme reaching this $4n^2$ average path-length enhancement, which is often called the Yablonovitch limit or the Lambertian limit. Luque and Miñano, and later Rau *et al.*, showed that the $4n^2$ Lambertian limit is actually the average path-length enhancement limit only when considering—and, hence, averaging over—all angles of incidence.^{10–12} Therefore, the

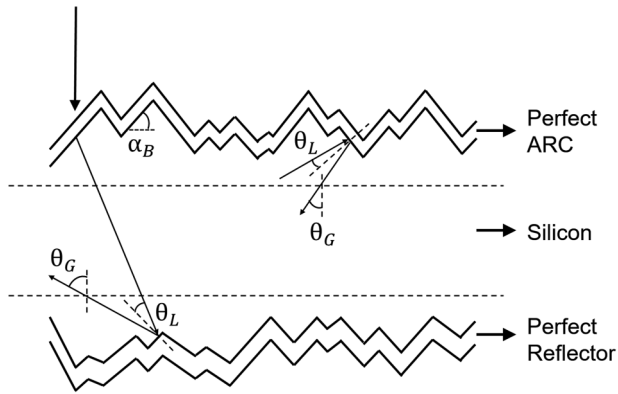


FIG. 1. Illustration of a textured silicon wafer showing the base angle (α_B) of the pyramids and the global (θ_G) and local (θ_L) angles with which rays traverse the wafer. Horizontal dashed lines are imaginary planes parallel to the macro-scale wafer surface. The global angle is defined relative to these planes. Conversely, the local angle is defined at the microscopic scale, relative to the pyramid facets.

path-length enhancement can be greater than $4n^2$ for a subset of angles of incidence, but at the expense of a reduced path-length enhancement at other angles such that the $4n^2$ limit is not violated.^{11,13} This behavior can be implemented with geometric concentration or angle selectivity schemes. Thus, the actual limit of the average path-length enhancement is^{10,12,13}

$$L = \frac{4n^2 w}{\sin^2(\theta_{in})}. \quad (1)$$

Here, θ_{in} is the acceptance angle of the angular-selective filter or the angle associated with the concentration factor.

No measured or simulated non-random texture has exceeded the Lambertian limit over a wide range of incident angles and photon wavelengths. Of particular importance, Brendel demonstrated that the simulated average path-length enhancement of ideal-random pyramids under isotropic illumination can also approach $4n^2$, but this does not ensure that ideal-random pyramids and Lambertian surfaces will yield the same short-circuit current densities since the distribution of path lengths can be (and is) different.⁸ In an earlier contribution, Campbell and Green had found that the fraction of rays that remain trapped in a wafer with ideal-random pyramids (but of identical size) approaches that of a wafer with Lambertian surfaces after approximately four passes through the wafer.⁵ However, it is not just the number of trapped rays that determines the path-length enhancement but also the angles with which they traverse the wafer. This missing information can be conveyed by plotting the angular distribution function (ADF) of a packet of rays inside the wafer and tracking how it evolves over time as those rays scatter at the front and rear surfaces.

Another piece of information that is missing from the silicon light-trapping literature is how the non-idealities of real pyramids affect the expected path-length enhancement. Studies have shown that, depending on the etchant type, etching time, and age and

temperature of the chemical bath, a range of pyramidlike texture morphologies are possible.^{14–16} The observed differences are in the height and shape of the pyramids, and, more importantly, in their base angle.^{15,17–19} Scanning electron microscopy (SEM) and atomic force microscopy (AFM) analysis of random pyramids have revealed base angles between 49° and 53° .^{2,15,18,20} Similarly, several different dominant base angles (50.5° , 51° , 52°) have been estimated from angle-resolved reflectance measurements,^{15,17} and dominant base angles between 47.9° and 54.3° were reported by Mackel *et al.* for a range of samples measured using confocal laser scanning microscopy.¹⁹ These observations have been implemented in simulations in which a single base angle, usually below 54.7° , is chosen so as to accurately reproduce the measured total front-surface reflectance (for wavelengths <1000 nm) of a given random-pyramid wafer.^{17,19,21,22} However, the single-base-angle approach fails to reproduce the distribution of angles observed experimentally in angle-resolved reflectance measurements. Baker-Finch *et al.* found that the broad angle-resolved reflectance of two wafers textured with different recipes could be described by Gaussian distributions of base angles with centers at 50.5° and 52.1° and full width at half maximums of 4.8° and 2.5° , respectively.¹⁷ Yang *et al.* found similar evidence in two-dimensional reflectance patterns, concluding that their sample had a distribution of base angles with an average value of 51° .¹⁸ Another shortcoming of simulating random pyramids with a single base angle model is that it does not capture the superior absorptance measured in textured silicon, especially at long wavelengths.²⁰ Recently, Fung *et al.* and Höhn *et al.* showed that additional scattering, in the form of a Phong scatterer (the properties of which were empirically fitted to measured results), should be added to the single-base-angle model to match the measured absorptance of long wavelength (1000–1200 nm) light.^{20,23–25} These studies reveal a need for base-angle distributions in rigorous light-trapping simulations of cells, but this has not yet been reported in the literature.

It is also important to consider a distribution of base angles when analyzing the light-trapping performance of modules.^{18,23,24,26} For example, the angle at which light is reflected from the front surface of a solar cell, which depends on its texture, determines which encapsulant refractive index maximizes the fraction of light that experiences total internal reflection (f_{tir}). An initial simulation study that assumed a single pyramid base angle suggested that f_{tir} could be improved from 3% to 80% by increasing the encapsulant refractive index from 1.50 to 1.59. However, Yang *et al.* and others found that the f_{tir} gain is more modest ($<16\%$), even for a wider encapsulant refractive index range (1.50–2.0), when considering the much broader distribution of angles in reflected light resulting from a distribution of base angles.^{18,27}

In this contribution, we investigate light trapping in wafers textured with randomly distributed pyramids having a (measured) distribution of base angles, which are referred to as “real-random” in this paper. We compare the results to those obtained with ideal-random pyramids and Lambertian surfaces. To this end, we accurately measure the topography of the surface of alkaline-textured silicon wafers with atomic force microscopy (AFM). The resulting real-random pyramid maps—along with ideal-random pyramid maps that are mathematically “reconstructed” from the measured topographies using 54.7° base angles—are ray-traced to probe their light-trapping capability. Throughout the simulations, we record

the ADF of the rays each time they hit the front or rear internal surface of the wafer; the ADFs conveniently contain all information about light trapping. There are, in fact, two ways to report ADFs, and each method is valuable. The “global ADF” (G-ADF) gives the rays’ trajectories with respect to the wafer normal—the global angle (θ_G), as shown in Fig. 1. As it tracks the angles at which rays travel from the front to rear surface and vice versa, the global ADF can be used to calculate the average path-length enhancement and total absorption in the wafer, provided the number of rays remaining is known at each pass. The “local ADF” (L-ADF) gives the rays’ trajectories with respect to the normal of the pyramid facets—the local angle (θ_L), also shown in Fig. 1—and strongly depends on the pyramid base-angle distribution. The local ADF at the front surface determines the transmission of light out of the wafer (hereafter termed “escape reflection” because it contributes to the reflected light in a measurement). Similarly, the local ADF at the rear surface determines the absorption in the rear contact of a solar cell; the structures simulated here have perfect rear reflectors, but real cells suffer from parasitic absorption that depends on local angle.^{28–30} Both escape reflection and parasitic absorption reduce the number of rays remaining in the wafer and, thus, the average path-length enhancement.

II. EXPERIMENTAL

A. Measurements

Monocrystalline silicon wafers with (100) orientation and either random or inverted-pyramid textures—both formed by alkaline etching—were provided by commercial silicon solar cell manufacturers. From these wafers, realistic topographical maps of real-random pyramids and real-inverted pyramids were generated. Optical profilometry and scanning electron microscope (SEM) stereoscopic image reconstruction were considered as methods to measure the topography, but both were found to lack the necessary nanometer-scale spatial resolution required to resolve the sharp peaks and valleys of pyramids. AFM was chosen instead, and measurements were performed in the tapping mode to avoid tip breakage when scanning over large areas with dramatic changes in height. To accommodate the tallest pyramids of the samples, which were over $7\mu\text{m}$ in height, an NT-MTD AFM with a z-range of $12\mu\text{m}$ was employed.

Particular attention was given to choosing the best-suited AFM tip, which was found to be a $>10\text{-}\mu\text{m}$ -tall, sharp, single-crystal diamond tip from SCD Probes. This tip reliably reproduced the pyramid base angles and avoided flat spots in the scans, which can arise if the cantilever hits the top of pyramids, thus stopping the tip from reaching the valleys. Prior to measurement, z (height) and x-z (sidewall angle) calibrations were performed using 0.11-, 0.52-, and $1.4\text{-}\mu\text{m}$ -tall standards and a 70° edge-angle standard, all from K-TEK Nanotechnology. For all measurements, the scanned area was sufficiently large ($40 \times 40\mu\text{m}^2$) to be representative of the overall surface. In particular, each scan included approximately 100 peaks for random pyramids and 25 peaks for inverted pyramids—enough to accurately capture the distribution of base angle, the variation of pyramid height, and the randomness of the pyramid positions.

The measured real-random and real-inverted-pyramid AFM maps served as input into a custom MATLAB code to create ideal-random pyramid and ideal-inverted-pyramid maps by changing

the base angle of all pyramids to 54.7° while keeping their peak positions and heights the same. The algorithm first finds the pyramid peaks in the input map and then constructs a new map by reducing (or increasing, for inverted pyramids) the height of the neighboring pixels according to the desired base angle. This process is repeated until neighboring pyramids intersect. The resulting map has a very narrow distribution around the desired base angle, but it is not quite a delta function, as an unintended consequence of the methodology is that the points at which adjacent pyramids intersect can have slightly different base angle than the desired value.

For select samples, AFM measurements were complemented with scanning electron microscopy (SEM) images of cross sections cut with a focused ion beam (FIB). Sequential imaging and milling were done with an FEI Nova 200 by pointing the FIB and SEM columns at the same point (the eucentric point) on the wafer. Milling was performed with a gallium ion beam oriented perpendicular to the wafer and rastered parallel to (two of the four) pyramid base edges. SEM images were taken at 52° from the wafer normal. Before milling, the pyramids were coated with 200 nm of platinum to protect the pyramid profiles and to provide contrast that simplifies subsequent image processing.

The pyramid base angle distribution of select samples was calculated from AFM scans using Gwyddion, a data analysis program, and from SEM images of milled cross sections using image processing tools in MATLAB. Before calculating base angle distributions, the images were oriented such that the x and y directions were aligned with the pyramid base edges, and the z direction was aligned with the wafer normal. In Gwyddion, a plane was fit at each pixel and the magnitude of its gradient—the base angle—was calculated. In MATLAB, a pixel intensity threshold filter was used to find the profile of the pyramids, which appear dark and are capped with platinum that appears bright. A line was then fit at each pixel along the profile through 50 neighboring points, which corresponds to a physical distance of $1.35\mu\text{m}$, and its slope—the base angle—was calculated.

The total front-surface reflectance of textured wafers was measured over the 300–1000 nm wavelength range using a PerkinElmer Lambda 950 spectrophotometer equipped with an integrating sphere. The angle of incidence was 7° from the wafer normal. The angle-resolved reflectance was measured using an Automated Reflectance/Transmittance Analyzer (ARTA) that connects to the spectrophotometer.³¹ For these measurements, 270 nm light was incident at angles ranging from 0° to 20° relative to the wafer normal. For each angle of incidence, an integrating sphere detector mounted on a goniometer circled the sample in the horizontal plane, recording the reflectance every 2° . Note that the angle-resolved reflectance cannot be measured for detector angles between -12° and $+12^\circ$ because the reflected light is blocked by the incident light source. The aperture width of the detector was 5° for all measurements. The wafers were oriented such that (two of the four) base edges of each pyramid, as well as the wafer normal, were coplanar with the circle traced by the detector.

B. Simulations

Optical simulations were performed with an optical simulator named CROWM (combined ray optics/wave-optics model) that has

been previously used to study the optical properties of solar cells.^{30,32,33} CROWM is capable of performing three-dimensional incoherent ray tracing based on geometric optics, as well as transfer-matrix calculations for thin films included in the simulation domain. Simulations were carried out for air/silicon/perfect-reflector structures with the top and bottom surfaces of the silicon having a pyramid texture measured by AFM (real-random and real-inverted) or reconstructed from such measurements (ideal-random and ideal-inverted). The thickness of the silicon wafer was 180 μm for all simulations, and free-carrier absorption was not included. Note, however, that such parasitic absorption can become important when accurately modeling light trapping beyond 1200 nm wavelengths and in solar cells that contain heavily doped regions.^{34,35} Encapsulant layers were not included in the simulations, as they change the escape cone of light within the wafer only slightly. Periodic lateral boundary conditions were enforced by mirroring the textures across first the x axis and then the y axis. The front-surface reflection spectrum of each texture was simulated for the 300–1000 nm wavelength range, with a 10 nm step, for light incident at 7° with respect to the wafer normal (as in the spectrophotometry measurements). Also simulated was the angle-resolved reflectance for 270 nm light having an angle of incidence between 0° and 20°. As in the measurements, a simulated detector was swept across angles between −90° and 90° with respect to the incident beam, in the plane perpendicular to the wafer surface and the pyramid base edges. The aperture width of the simulated detector was 5°.

Next, local and global ADFs were collected for each pass through the wafer by monitoring each ray of the normally incident 1200 nm light. This wavelength was chosen because the absorption in silicon is negligible. For these simulations, we implemented perfect transmission of incident rays and rays hitting the front surface within the escape cone from inside the silicon; this is equivalent to having a perfect antireflection coating. Rays were binned in 0.5° increments according to their angle (0°–90°) with respect to either the appropriate pyramid facet (local ADF) or the wafer normal (global ADF). The ADFs were then normalized at each pass by dividing by the total power of the remaining rays. Lastly, the total path-length enhancement was investigated as a function of the angle of incidence of 1200 nm light for angles between 0° and 75°, with a 5° step. The wavelength was kept constant at 1200 nm. The total path length enhancement was calculated by dividing the total distance traveled by all 10 000 rays by the total number of rays and expressing the result in terms of the wafer thickness.

III. RESULTS AND DISCUSSION

A. AFM map validation

Obtaining an accurate topographical map with AFM is not a trivial task for samples containing both micrometer- and nanometer-scale features. Challenges that we encountered, particularly over large-area scans, include tip-related artifacts, rounded edges of pyramids, and artificial flat spots.^{36,37} Consequently, we verify the fidelity of the AFM height maps prior to light-trapping analysis using measurements and simulations of the total and angle-resolved reflectance, as described in detail below. We begin this verification process with inverted pyramids and then move on to random pyramids. While inverted pyramids are not the primary

focus of this paper, they serve as a convenient test case or standard for the verification methodology because they have less randomness in pyramid height, position, and base angle than random pyramids, making them easier to analyze.

Figure 2(a) shows an AFM scan of real-inverted pyramids approximately 9 μm in depth, and Fig. 2(d) reveals the pyramid base angle distribution calculated from this map. There are two dominant peaks in the distribution curve—at 54.1° and 55.3°—with an average of 54.7°, the expected base angle for anisotropic etching of silicon. The appearance of two peaks may be the result of a slight (0.6°) sample tilt during measurement, leading to a splitting of the measured angles for the leading and trailing edges of pyramids. Alternatively, the wafer may have been 0.6° off-cut from the intended (100) orientation prior to texturing—this is just at the orientation tolerance specified by most wafer manufacturers—resulting in pyramids that are in fact slightly tilted.⁴ The small peak at 0° originates from flat spots between the inverted pyramids—visible in Fig. 2(a)—that result from the photolithographic masking process used to define the location of each inverted pyramid.

As a preliminary check of the base-angle distribution extracted from AFM, the inverted-pyramid sample was progressively milled parallel to the (010) plane with a FIB, and SEM images were taken of each cross section. Three such cross sections are displayed in Fig. 2(c). The associated calculated base-angle distribution, displayed in Fig. 2(d), is slightly broader than that from AFM (note the very different data processing used to extract these angles), but contains the same split peak and an average value of 54.7°. Similar values were reported for inverted pyramids by Yang *et al.* and Baker-Finch *et al.*^{17,18} Also shown in Fig. 2(d) is the base-angle distribution of the ideal-inverted-pyramid map in Fig. 2(b), which was reconstructed from the measured map in Fig. 2(a). As intended, ideal-inverted pyramids present a unique narrow peak centered around 54.7°.

In Fig. 3(a), the measured reflectance spectrum of the inverted-pyramid sample is compared with the simulated spectra from real-inverted pyramids—i.e., that obtained by ray tracing the map in Fig. 2(a)—as well as from ideal-inverted pyramids, mapped in Fig. 2(b). Assuming the AFM map to be an accurate reproduction of the actual surface morphology and the features to be sufficiently large to use geometric optics,^{38,39} we expect ray-tracing simulations to precisely reproduce the optical response of the sample. Indeed, the simulated real-inverted pyramids' reflectance is in relative agreement with the measured data above 400 nm, leading to an AM1.5G-weighted average reflectance difference of only 0.2% (higher). This compares with a difference of 1.3% (lower) for the simulated ideal-inverted pyramids, in large part due to the elimination of flat spots during the construction of the ideal-inverted-pyramid map.

The measured AFM map can be further validated using angle-resolved reflectance measurements. The detector angle at which the peak reflectance is measured for normally incident light ($\theta_{r,peak}$) varies with the prevalent pyramid base angle ($\alpha_{B,peak}$) according to

$$\theta_{r,peak} = 4\alpha_{B,peak} - 180^\circ, \quad (2)$$

with $\theta_{r,peak}$ and $\alpha_{B,peak}$ in degrees.¹⁷ The angle-resolved reflectance is, thus, a sensitive probe of base angle: for each 1°

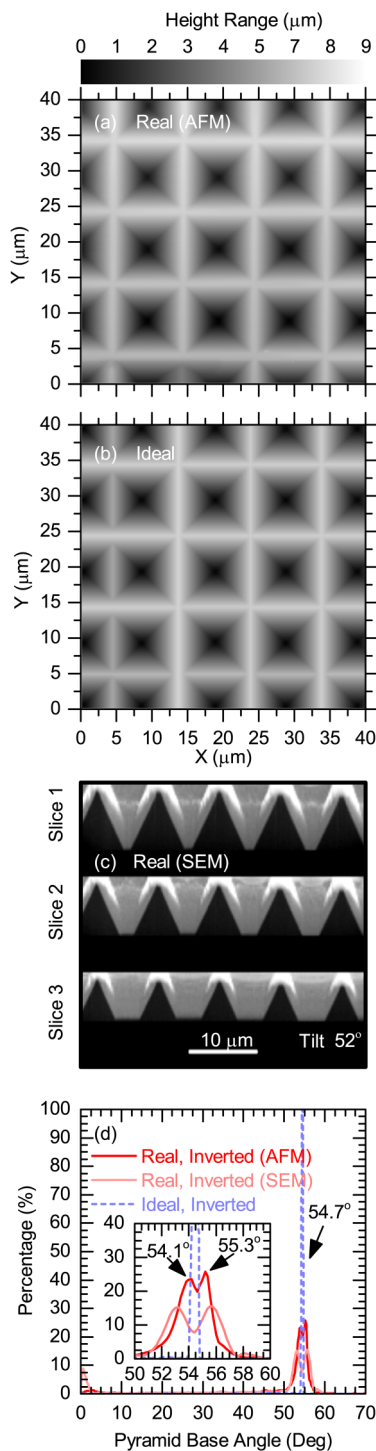


FIG. 2. (a) AFM map of an inverted-pyramid wafer (*real-inverted*). (b) Reconstructed map from (a) with ideal-inverted pyramids (*ideal-inverted*). (c) SEM cross sections of successive slices of real-inverted pyramids, milled with FIB. (d) Base-angle distributions of inverted pyramids.

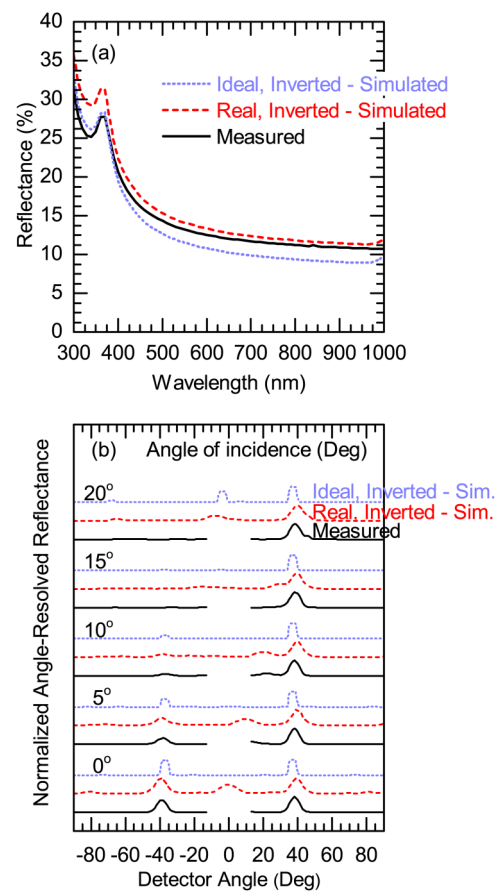


FIG. 3. (a) Spectrally resolved reflectance and (b) angle-resolved reflectance from the simulation of ideal-inverted pyramids, simulation of real-inverted pyramids, and experimental spectrophotometry measurement. A noteworthy feature of the curves is the presence of the specular peak (detector angle equal to twice the angle of incidence) for simulated real-inverted pyramids and the measured data, while this peak is absent for ideal-inverted pyramids. Otherwise, the angles at which peaks occur match for all three curves within $\pm 2.5^\circ$.

variation in base angle, the angle at which the most light is reflected shifts by 4° .

Figure 3(b) compares the measured angle-resolved reflectance to that obtained by ray tracing the real- and ideal-inverted-pyramid maps, for several angles of incidence. In the simulated ideal-inverted-pyramid case at 0° incidence, the peak scattering angle lies at $\pm 39.5^\circ$, corresponding to a base angle of 54.9° , in close agreement with the ideal base angle of 54.7° . We assume a 5° detector aperture in our simulations in order to match the experimental setup; hence the flat-top profile of the reflectance peaks for ideal-inverted pyramids as seen in Fig. 3(b). As expected, the measured data presents peaks at a nearly identical scattering angle of $\pm 39^\circ$, as real pyramids exhibit the same average base angle as the simulated ideal-inverted pyramids. However, the peaks are broader and rounder, due to the non-ideal distribution in base angles shown in Fig. 2(d). The simulated peak scattering angle from real-inverted pyramids differs from the

measured value by less than 1° , setting an upper bound of 0.25° for the error in the base angle of the AFM map. Some of this error may also arise from a difference in granularity: the angle-resolved reflectance was acquired with 2° steps, whereas the simulations were performed with 0.1° steps. The accuracy of the AFM map was confirmed for all the angles of incidence displayed in Fig. 3(b).

This validation process was next carried out on random pyramids—the primary texture type of interest in this paper. Figure 4(a) shows an AFM map of the surface of a silicon wafer textured with random pyramids, with a maximum pyramid height of approximately $11\ \mu\text{m}$. The base angle distribution for this map, shown in Fig. 4(c), reveals a peak at 48.9° , considerably lower than the 54.7° theoretical value assumed in some optical simulations of solar cells.^{1,2} Moreover, the distribution is much broader than for real-inverted pyramids [Fig. 2(d)], and, when fitted with a Gaussian function, has a center at 48.9° and full width at half maximum (FWHM) of 2.3° . For comparison, Fung *et al.* reported Gaussian-fit random pyramids with a center at 50° and FWHM of 3.3° , also determined from AFM,²⁰ and Baker-Finch *et al.* reported Gaussian-fit random pyramids with centers at 50.5° and 52.1° with FWHMs of 4.8° and 2.5° , respectively, determined by fitting angular reflectance data.¹⁷ These average angles are slightly higher, which likely results from differences in the texturing chemistries used, but the widths of the distributions are similar. In Fig. 4(b), the ideal-random pyramid map reconstructed from the real-random pyramid map is displayed, with all base angles equal to 54.7° , as shown in Fig. 4(c).

The total reflectance spectra measured from the sample and simulated from the real-random and ideal-random pyramid maps are compared in Fig. 5(a). The reflectance simulated from the real-random pyramids has the same profile as the measured reflectance, but with a constant offset of approximately 0.9%. This may be attributed to the finite size of the AFM tip—which rounds sharp features such as peaks and edges—or it may be caused by diffraction from peaks and valleys that are not reproduced with ray optics simulations.³⁸ In particular, Haug *et al.* found that ray tracing can reproduce the scattering profile from pyramids along the principle axis (the axis parallel to the base of the pyramids) but fails to predict scattering happening due to features along the diagonal direction connecting the peaks of the pyramids (the axis diagonal to the principal axis), and it is only with a wave-optics approach that such diffractive effects can be correctly accounted for. The simulated reflectance from the ideal-random pyramids map is less representative of the actual sample: the reflectance is approximately 1.5% lower throughout the considered wavelength range. This behavior is expected, since real-random pyramids are flatter than ideal-random pyramids, leading to increased reflection.

In Fig. 5(b), the measured angle-resolved reflectance and simulated reflectance from real-random and ideal-random pyramid maps are compared. Because of their broad base-angle distribution [Fig. 4(c)], real-random pyramids result in broad reflectance peaks in both the measured and simulated cases. For an angle of incidence of 0° , the peak reflection is measured at a detector angle of $\pm 17^\circ$, which corresponds to a pyramid base angle of 49.3° . In comparison, simulated data from the real-random pyramid map exhibit a peak at $\pm 18.5^\circ$, corresponding to pyramid base angle of 49.6° . This compares with a prevalent base angle of 48.9° in the actual sample, as

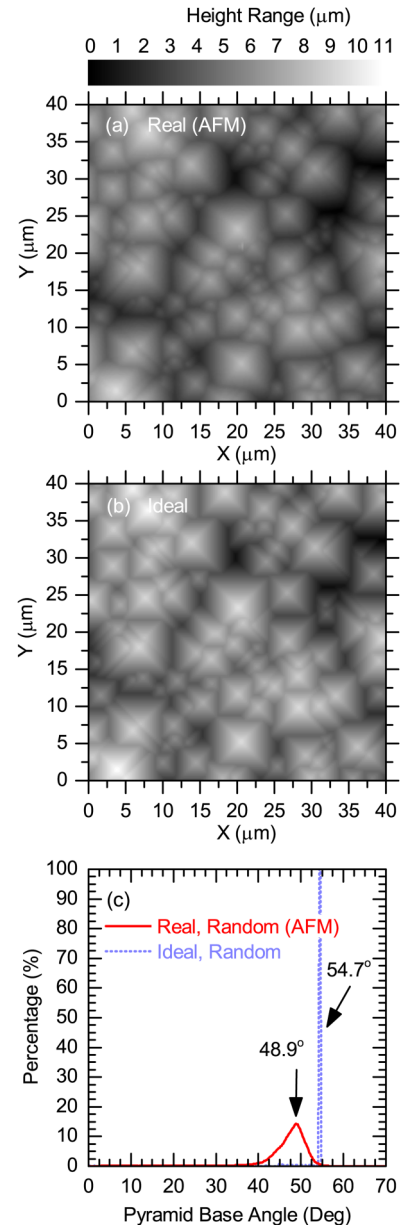


FIG. 4. (a) AFM map of a random-pyramid wafer (*real-random*). (b) Reconstructed map from (a) with ideal-random pyramids (*ideal-random*). (c) Base-angle distributions of random pyramids.

extracted from the AFM map [Fig. 4(c)]. These are all within 0.7° of each other, suggesting that AFM mapping and ray-tracing simulations do not introduce artifacts that misrepresent the actual pyramids. By contrast, simulations from the ideal-random pyramids map lead to a reflectance peak at $\pm 39.5^\circ$, as expected from our analysis of ideal-inverted pyramids. This emphasizes how inaccurate it can be to assume a 54.7° pyramid base angle when simulating the optics of silicon solar cells.

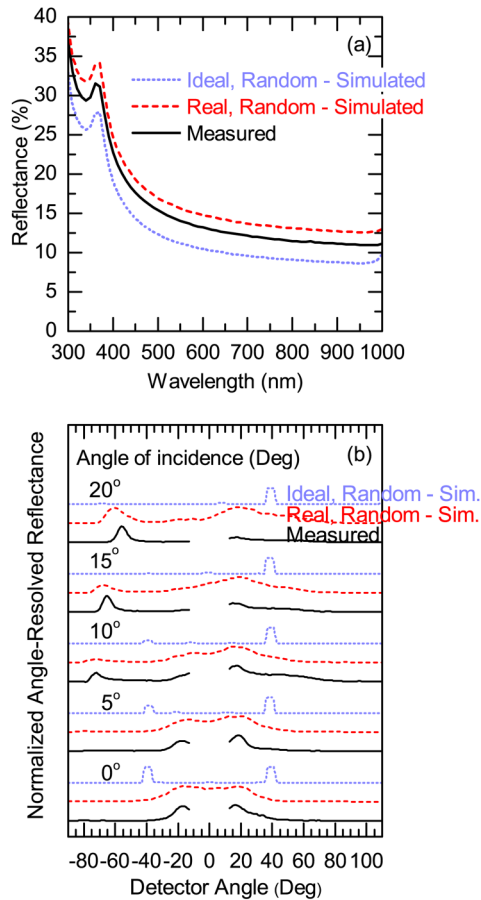


FIG. 5. (a) Spectrally resolved reflectance and (b) angle-resolved reflectance from the simulation of ideal-random pyramids, simulation of real-random pyramids, and experimental spectrophotometry measurements.

With increasing angle of incidence, the reflectance peaks measured and simulated from the real-random pyramid map change in concert, though the deviation increases (see, for example, the peak near -60° at an angle of incidence of 20°). We hypothesize that this is attributable to electromagnetic effects, as explained by Pla *et al.*³⁹ These authors found that the wavelength-to-period ratio—the period being the projected spacing between adjacent pyramids—becomes larger as the sample is tilted and as the area of the pyramids, projected perpendicular to the incident wavevector, decreases. This moves the sample from the regime of geometric optics to that of wave-optics, and, thus, the accuracy of ray-tracing methods decreases.

B. Comparison of real-random pyramids with a Lambertian scatterer

1. Angular distribution function

Having verified that precise AFM measurements yield an accurate height map of the random pyramids, we perform ray-tracing simulations of a monocrystalline silicon wafer using this map—and

the corresponding reconstructed ideal-random pyramid map—for both the top and bottom surface textures. Note that the results apply to the particular random-pyramid sample characterized above—and this sample is not strictly representative of all random-pyramid samples—but we believe the conclusions to be broadly applicable. Unless specified otherwise, the simulations are carried out for normal incidence of light. A packet of rays is traced *inside* this textured wafer to explore the (experimentally inaccessible) evolution of the light, and, in particular, the randomization of ray directions following scattering at each surface. We describe this randomization process with a normalized two-dimensional angular distribution function [ADF(θ, ϕ)] that gives the relative light intensity as a function of the polar (θ) and azimuthal (ϕ) angles in spherical coordinates. We then condense this information into a unidimensional polar ADF(θ) by integrating over ϕ ,

$$\text{ADF}(\theta) = \int_0^{2\pi} \text{ADF}(\theta, \phi) \sin(\theta) d\phi. \quad (3)$$

We then compare the resulting ADF(θ) to that of a Lambertian scatterer, given by:

$$\text{ADF}_{\text{Lambertian}}(\theta) = \int_0^{2\pi} \frac{1}{\pi} \cos(\theta) \sin(\theta) d\phi. \quad (4)$$

From here onwards, “ADF” refers to the unidimensional polar ADF(θ), unless specified otherwise. As mentioned in the Introduction, two ADFs are of interest: the global ADF (G-ADF) and the local ADF (L-ADF), which are defined with reference to the wafer normal and pyramid facet normal, respectively. Both G- and L-ADF can be reported in two manners. A “differential” ADF describes the angular distribution of rays at the end of a given pass, like a snapshot in time. Recording differential ADFs for successive passes thus elucidates how an initial packet of rays scatters inside the wafer over time. The “cumulative” ADF, on the other hand, is the sum of the differential ADFs over an infinite number of passes, weighted by the number of rays remaining within the wafer after each pass. Cumulative ADFs, thus, describe the total light intensity scattered into a given angle over the course of a large number of passes. Since the initial passes include the largest number of rays—for example, for a Lambertian scatterer, $1/\pi^2$ rays escape out the front surface per pass—the initial scattering events are represented strongly in cumulative ADFs.

Figures 6 and 7 display the differential G-ADF and L-ADF, respectively, for the first seven interactions with surfaces (the initial transmission and the six following reflections), as well as the cumulative ADFs. These are shown for real- and ideal-random pyramids, as well as a reference Lambertian scatterer. In these figures, “Pass” represents the number of one-way through-passes completed by the rays—i.e., from the top to the bottom surface, or from the bottom to the top surface. The ADFs for Passes 0–6 are, thus, differential ADFs, while the Pass ∞ plot at the bottom of each figure corresponds to the cumulative ADF. As these ADFs are normalized at each pass by the total light intensity remaining in the wafer, they can be compared regardless of the light escaping between passes. The transmittance ADFs (Pass 0) show the global (Fig. 6) and local (Fig. 7) angles at which light rays enter the wafer, and thus reveal how efficient different textures are at

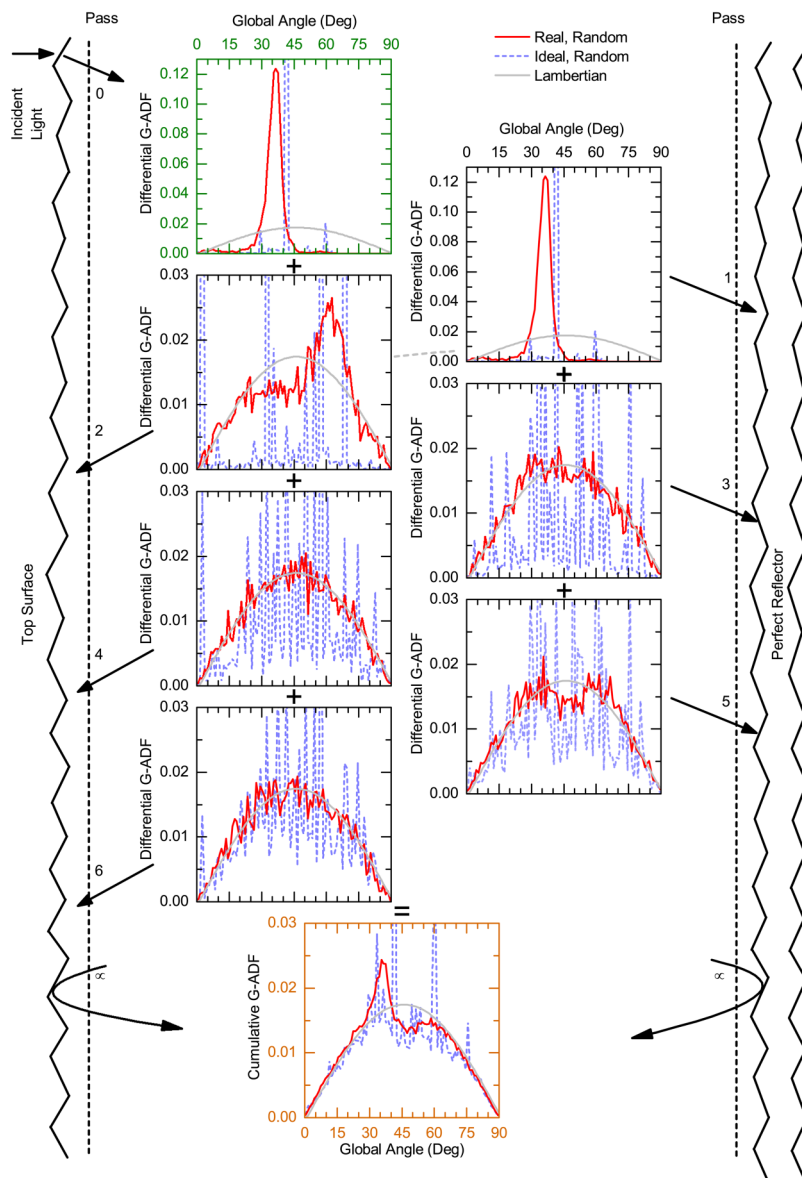


FIG. 6. Evolution of the global angle distribution function (G-ADF) as normally incident light rays that are trapped in the wafer make multiple passes between the front and rear surfaces. The first seven plots show differential G-ADFs, which are snapshots in time that capture the randomization of rays after a particular pass. The vertical dashed lines on each side of the wafer are imaginary planes defined to record the global angles at which trapped rays travel through the wafer. The first plot, for Pass 0, shows the G-ADF of light rays that have just been transmitted into the wafer. The following differential G-ADFs are reported just before the rays hit the surface. Thus, Passes 1, 3, and 5 show G-ADFs of the rays traveling down from the top surface and about to hit the bottom surface, while Passes 2, 4, and 6 show G-ADFs of rays about to hit the top surface. The last plot shows the cumulative G-ADF—weighted by the number of rays remaining within the wafer at each pass—for a large number of passes. Thus, this last plot is indicative of the total path-length enhancement.

scattering the incoming light through the rough front interface. For the following pass, the ADFs are recorded immediately before the reflection event (i.e., at the “end” of the pass; the L-ADFs of light rays *after* reflection and thus at the beginning of the next pass are in the [Appendix](#)). Hence, odd passes (1, 3, and 5) correspond to rays traveling down from the top surface and about to hit the bottom surface and, conversely, even passes (2, 4, and 6) correspond to rays traveling up from the bottom surface and about to hit the top surface. As a result, the G-ADFs ([Fig. 6](#)) for Pass 0 and 1 are the same, since the global angle ADF does not change between the initial transmission and the first reflection. Note, though, that this is not true from a local perspective, as shown by the L-ADFs ([Fig. 7](#)).

The ADF at Pass 0 is arguably the most important in maximizing the path length of light, as none has yet been lost to parasitic absorption in the back reflector or escape reflection through the front surface. As shown in [Fig. 6](#), the G-ADF for Pass 0 exhibits peaks at 41.5° and 36.5° for ideal-random and real-random pyramids, respectively, thus offering a greater path length for the former. In a $180\text{-}\mu\text{m}$ -thick silicon absorber, considering light in the $1000\text{--}1200\text{ nm}$ wavelength range, this difference in first-pass path length would lead to 0.13 mA/cm^2 additional photocurrent generated during the first pass with ideal-random pyramids.

It thus appears that the smaller base angles of real-random pyramids are detrimental, as they reduce the path length of the first pass compared with ideal-random pyramids. However, as we show

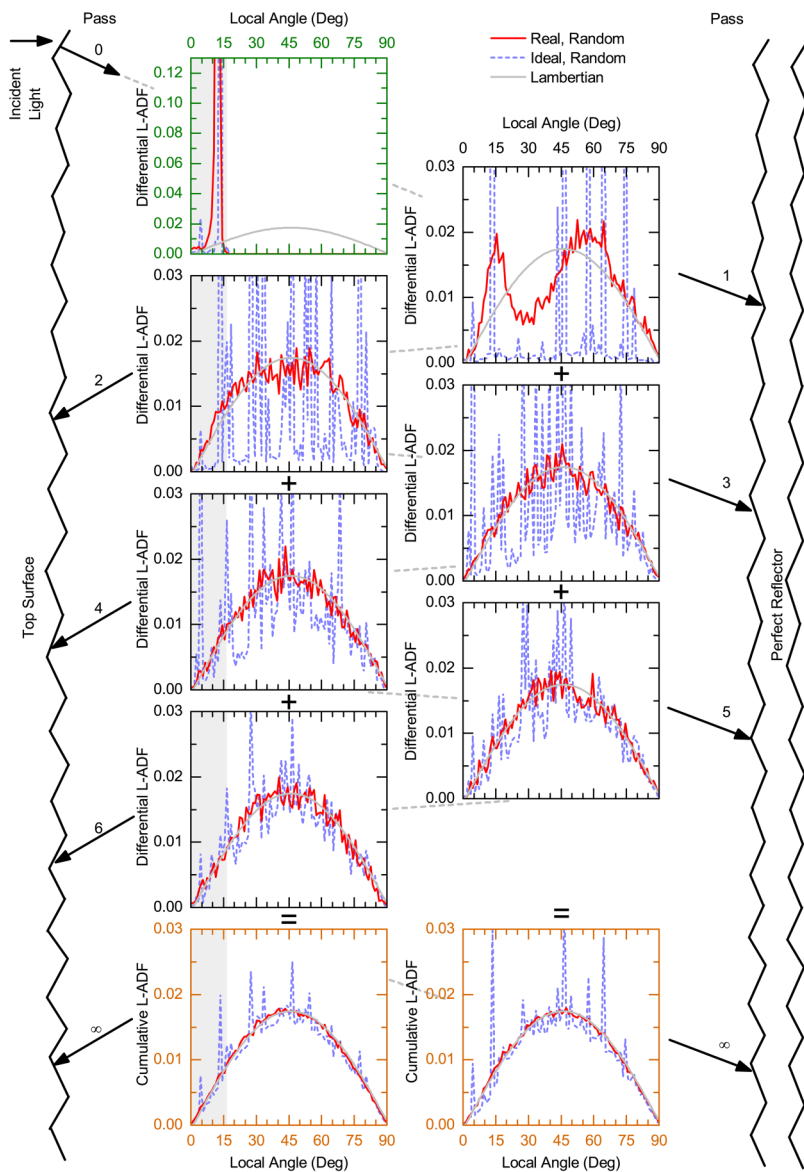


FIG. 7. Evolution of the local angle distribution function (L-ADF) as normally incident light rays that are trapped in the wafer makes multiple passes between the front and rear surfaces. The first seven plots show differential L-ADFs, which are snapshots in time that capture the randomization of rays after a particular pass. The first plot, for Pass 0, shows the L-ADF of light rays that have just been transmitted into the wafer. The following differential L-ADFs are reported just before the rays hit the surface. Thus, Passes 1, 3, and 5 show L-ADFs of the rays traveling down from the top surface and about to hit the bottom surface, while Passes 2, 4, and 6 show L-ADFs of the rays about to hit the top surface. The last two plots show cumulative L-ADFs for the top and bottom surfaces, respectively. Cumulative L-ADFs are computed by summing the differential L-ADFs for the respective surface—weighted by the number of rays remaining at each pass—for a large number of passes. The cumulative L-ADF for the top surface is thus indicative of the total light that falls into the escape cone (shaded angles) and contributes to escape reflection. Similarly, the cumulative L-ADF for the bottom surface is indicative of the total parasitic absorption in the back reflector.

hereafter, the *distribution* of base angles is an advantage, as it is more efficient in randomizing the light. This can be seen in the G-ADF for Pass 1: ideal-random pyramids exhibit a narrow peak, whereas real-random pyramids have a broader peak. As a result, light rays hit the back surface with a wider distribution of angles for real-random pyramids. This is also visible in Fig. 7: the L-ADF for ideal-random pyramids is a concatenation of narrow peaks, whereas real-random pyramids lead to a broad ADF covering the full 90°. Since the back surface of solar cells is engineered to be highly reflective (here we assume $R = 1$), the total light intensity is negligibly reduced between Pass 1 and Pass 2. Hence, the inferior Pass-1 path length with real-random pyramids can be counterbalanced during Pass 2. Indeed, the G-ADF for Pass 2 is broad for

real-random pyramids—representing substantial randomization of ray direction—whereas the G-ADF for ideal-random pyramids has sharp peaks at high angles (e.g., 57° and 68°) but also at very low angle (2°). Hence, a sizable portion of light travels back nearly perpendicular to the wafer. This light experiences barely any path-length enhancement.

This can also be inferred from the root mean squared deviation (RMSD) of the G-ADFs from Lambertian behavior, displayed after each pass in Fig. 8(a) and calculated according to

$$\text{RMSD} = \sqrt{\frac{\int_{\theta=0}^{\theta=\pi/2} (\text{ADF}(\theta) - \text{ADF}_{\text{Lambertian}}(\theta))^2 d\theta}{\pi/2}} \quad (5)$$

and the average path-length enhancement (PLE) *per pass*, shown in Fig. 8(c) and given by

$$\text{PLE} = \int_0^{\pi/2} \text{ADF}(\theta) \frac{1}{\cos(\theta)} d\theta. \quad (6)$$

For real-random pyramids, the deviation of the G-ADF from Lambertian is maximal for Pass 1, and it drops to near zero for subsequent passes [Fig. 8(a)]. As a result, real-random pyramids have a relatively low PLE of 1.23 for Pass 1, but the PLE reaches and maintains the value of 2—the PLE per pass of a Lambertian scatterer—by the second pass, as shown in Fig. 8(c).

In contrast, ideal-random pyramids exhibit a higher PLE of 1.34 for Pass 1, but the PLE remains lower than 2 for the next two passes. Unsurprisingly, both the G- and L-ADFs for ideal-random pyramids remain non-Lambertian until approximately Pass 8 (see Pass 6 in Figs. 6 and 7). Yet, the PLE per pass reaches 2 at Pass 4, thus demonstrating that the distribution of rays does not have to be Lambertian for the structure to perform as efficiently as a Lambertian scatterer. Similar results were reported by Boccard *et al.*⁴⁰ Their analytical model—which yielded good agreement between calculated and measured short-circuit current density and external quantum efficiency (EQE)—relies on a similar observation: they assumed non-Lambertian light scattering, with an average PLE per pass below 2 for the first round-trip through the absorber and a Lambertian ADF for subsequent passes. These results also validate the optical simulation approach used in the simple but effective PC1D software, which assumes Lambertian behavior of random pyramids after the initial passes.⁴¹

The cumulative G-ADFs (Pass ∞ , at the bottom of Fig. 6) capture the overall performance of the textures in terms of PLE per pass. The peaks from the initial transmission (Pass 0), at 41.5° for ideal-random pyramids and 36.5° for real-random pyramids, are still apparent, thus highlighting the importance of the first scattering event. More importantly, the cumulative G-ADFs show that, although both textures are eventually able to randomize the light, the common Lambertian assumption is not entirely true for either real-random pyramids or ideal-random pyramids. However, the distribution for real-random pyramids is markedly closer to the Lambertian model.

2. Escape reflection and parasitic absorption

In addition to maximizing the path-length enhancement through the wafer, light-trapping textures should minimize escape reflection by scattering rays away from the escape cone. As shown in Fig. 7, for both textures, the packet of light rays enters the wafer with a distribution of local angles within the escape cone (16.6° for the air/silicon interface—the shaded area), in agreement with Snell's law. However, after one round-trip back to the front surface (Pass 2), real-random pyramids scatter the rays away from the escape cone, with an angle distribution close to Lambertian. In comparison, the distinct peaks caused by the narrow base-angle distribution of ideal-random pyramids result in a substantial fraction of light reaching the front surface within the escape cone. In particular, the pyramid facets on the top and bottom surfaces of the wafer are parallel when the pyramids are ideal. Consequently, many of the rays that are initially transmitted into the wafer nearly

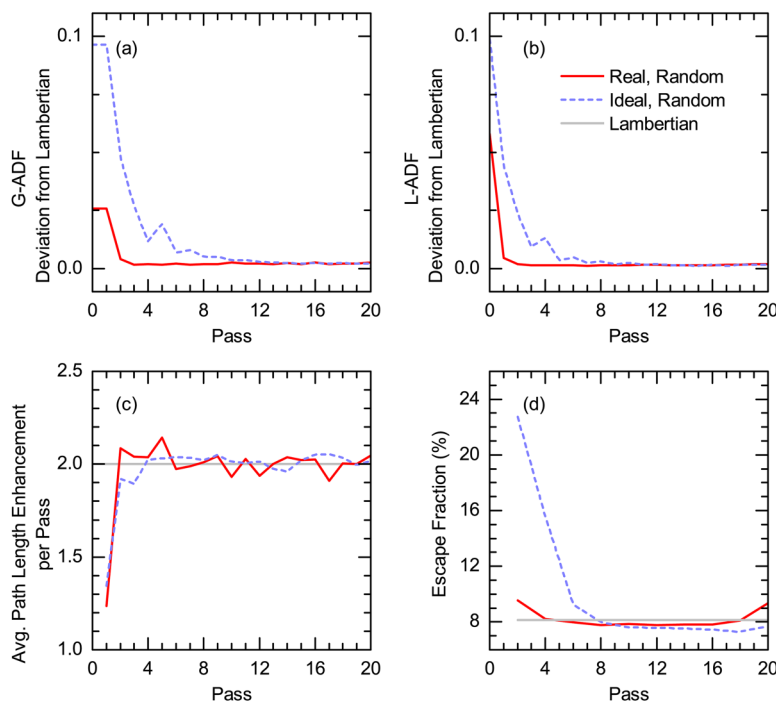


FIG. 8. Deviations of (a) global angle distribution function (G-ADF) and (b) local angle distribution function (L-ADF) from Lambertian behavior as a function of the number of passes of light through the wafer. These deviations are defined as the root mean square difference. (c) Average path-length enhancement per pass, calculated from the differential G-ADFs. (d) Escape fraction at each pass calculated from the differential L-ADFs. These results are for normal incidence of light.

perpendicular to a pyramid facet (Pass 0 in Fig. 7) arrive nearly perpendicular to a pyramid facet at the back surface and, finally, arrive again at the front surface nearly perpendicular to a pyramid facet, whereupon they escape. For real-random pyramids, the broader distribution of pyramid base angles strongly reduces the probability of such events. Thus, as shown in Fig. 8(b)—which displays the deviation of the L-ADFs from Lambertian, calculated using Eq. (5)—ideal-random pyramids take eight passes to achieve a Lambertian distribution, whereas it takes only two passes for real-random pyramids.

This difference in behavior is also apparent in Fig. 8(d), which shows the fraction of light escaping each time the rays reach the top surface, given by

$$R_{\text{escape fraction}} = \int_0^{\theta_c} T_{\text{ARC}}(\theta) \times L\text{-ADF}(\theta) d\theta, \quad (7)$$

with θ_c the critical angle and T_{ARC} the transmittance of the top surface. Here, we assumed $T_{\text{ARC}} = 1$ for angles of incidence within the escape cone, corresponding to a perfect antireflection coating. For a Lambertian scatterer, the fraction of rays that escape is $R_{\text{escape fraction}} = 1/n^2$, with n the refractive index of the absorber material. For silicon, $n = 3.5$ at near-bandgap wavelengths and $R_{\text{escape fraction}} = 8.2\%$ (per pass) with a Lambertian surface. In comparison, for ideal-random and real-random pyramids, the first internal reflection event on the front surface (Pass 2) leads to 22.7% and 9.6% of light rays transmitted through the escape cone, respectively. Considering light in the 1000–1200 nm range and a 180- μm -thick silicon absorber, these first escaped rays amount to 1.1, 0.45, and 0.37 mA/cm² photocurrent lost for ideal-random pyramids, real-random pyramids, and a Lambertian scatterer, respectively. For subsequent internal reflection events on the front surface (even Passes), the escape fraction remains consistent at $7.7 \pm 0.6\%$ for real-random pyramids. This compares to escape fractions of 15.6% for Pass 4, 9.3% for Pass 6, and $7.3 \pm 0.5\%$ for the following even Passes, for ideal-random pyramids. A Lambertian surface is thus an appropriate approximation of real-random pyramids for the purposes of calculating escape reflection—this is confirmed by the front-surface cumulative L-ADF (Pass ∞ in Fig. 7)—but ideal-random pyramids are dissimilar to both of these.

The final characteristic of an excellent light management scheme is minimal parasitic absorption. The rear-surface cumulative L-ADF, also in Fig. 7, determines parasitic reflection in the rear contact and reflector.^{28–30} For example, Holman *et al.* found that parasitic absorption in the silver layer of a silicon/indium-tin-oxide/silver stack is the highest when light arrives at a pyramid facet at the silicon/indium-tin-oxide critical angle (35°).²⁹ The L-ADF for Pass 1 is non-Lambertian for real-random pyramids, with conveniently few rays arriving near 35° (and at 25°, which is the critical angle for a lower-refractive-index silicon dioxide passivation layer). This effect is drowned out, however, by subsequent passes that leave the rear-surface cumulative L-ADF looking very similar to Lambertian. A Lambertian surface is thus also an appropriate approximation of real-random pyramids for the purposes of calculating parasitic absorption. Ideal-random pyramids provide a less accurate

approximation, and care must be taken if any of the prominent peaks occur at angles associated with strong parasitic absorption in a given contact.

3. Total path-length enhancement

Taken together, the path-length enhancement per pass, the escape reflection through the front surface, and the parasitic absorption in the rear reflector determine the total path-length enhancement. This common light-trapping metric is closely related to the total photogenerated current density. However, to compare the path-length enhancement of a given texture to the $4n^2$ Lambertian limit requires isotropic illumination, and, thus far, we have considered only normal incidence of light. Accordingly, Fig. 9 compares the average path-length enhancement for simulated real-random, real-inverted, ideal-random, and ideal-inverted pyramids for incident angles between 0° and 75°. Real-random and real-inverted pyramids both outperform the Lambertian scatterer at all incident angles below 55°. In comparison, ideal-inverted and ideal-random pyramids exceed Lambertian performance over narrower incident-angle ranges of 0° to 30° and 0° to 45°, respectively.

The large path-length enhancement in Fig. 9 at normal incidence at first appears counter-intuitive, as Figs. 6–8 revealed that real- and ideal-random pyramids are inferior to a Lambertian scatterer in terms of both average path-length enhancement per pass and escape reflection for the first couple of passes. However, both these textures provide a lower escape reflectance for later passes [as shown in Fig. 8(d)]. Thus, although more rays are lost early, and these rays travel a shorter path, the remaining rays are retained longer within the wafer, and hence, contribute to the greater average path-length enhancement. In addition, the cumulative G-ADF plot (Pass ∞) for ideal-random pyramids in Fig. 6 shows strong peaks at 60° and 75°, indicating that a non-negligible portion of the rays travels longer per pass than in the Lambertian case. This helps make up for the loss of rays in early passes.

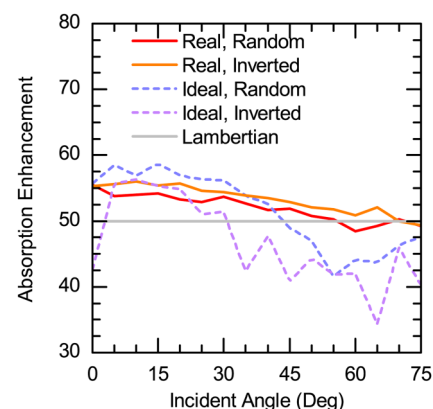


FIG. 9. Total path-length enhancement of the textures investigated, calculated at a wavelength of 1200 nm, for 5° steps in the angle of incidence.

Campbell *et al.* observed similar results when considering rays remaining in a wafer: ideal-regular and ideal-random pyramids lose more rays through escape reflection in early passes but, after enough passes, both textures retain more rays than a Lambertian scatterer, thus leading to comparable *average* path-length enhancement.⁵ Similar results were also reported by Brendel: at normal incidence, for some relatively simple texture schemes, average path-length enhancement values exceeding 100 are possible, which is considerably higher than the Lambertian limit.⁸ These same textures can outperform Lambertian scatterers for a restricted range of higher incident angles. This result is consistent with light-trapping physics, provided that, once averaged over the full range of incident angles (0° – 90°), the path-length enhancement remains below or equal to the $4n^2$ limit.^{10,12} For example, Campbell *et al.* showed that (ideal) perpendicular grooves can exceed the Lambertian limit when light is incident within 30° – 45° of the wafer normal,⁵ but Brendel simulated that this texture and others all achieve an average path-length enhancement of approximately $4n^2$ under isotropic illumination.⁸ Our results in Fig. 9 are consistent with these reports, demonstrating enhanced light trapping in random- and inverted-pyramid-textured wafers for select angles of incidence.

In contrast, using spectral photoluminescence techniques, Barugkin *et al.* claimed “light-trapping efficiencies” (LTEs) considerably *lower* than the Lambertian limit for different textures—including random pyramids—on silicon wafers. We attribute this difference to the definition used for “light trapping” and to the experimental apparatus used. The authors’ definition of LTE includes parasitic absorption contributions from accompanying layers, but the Lambertian light-trapping limit is defined as the path-length enhancement over the planar case in the absence of absorption.^{42,43} Schuster *et al.* have similarly calculated low LTE values when accounting for parasitic absorption.⁴² Moreover, during PL measurements, Barugkin *et al.* used a detached back reflector with reflectance $R > 95\%$. This lower bound on R is inadequate: it leads to considerable parasitic absorption and, consequently, low LTE values.⁴³ Indeed, Deckman *et al.* showed that, with just 6% parasitic absorption per pass, the absorption enhancement drops to half of the Lambertian limit.⁴⁴ If parasitic absorption is present, the correct procedure to calculate the light-trapping potential of a texture is to mathematically eliminate the parasitic absorption by dividing it between EQE and reflectance according to the method described first by the thin-film silicon community.^{45–47} Using this method, Holman *et al.* argued that the experimental EQE of a crystalline silicon solar cell with random-pyramid texture is very close to simulations assuming a Lambertian behavior,⁴⁸ consistent with the simulations in the present work based on measured texture maps.

IV. CONCLUSION

Understanding of the light trapping afforded by random-pyramid texture on crystalline silicon wafers has improved over the last three decades, and this work extended that learning by simulating the path of rays interacting with accurate three-dimensional height maps of textured silicon wafers. These maps revealed that random pyramids exhibit a wide distribution of base

angles with a peak below 54.7° , a theoretical value expected from anisotropic etching of the crystalline planes. Through ray-tracing simulations based on these *real-random* maps, as well as reconstructed *ideal-random* maps featuring ideal pyramids with 54.7° base angles, we demonstrated that the broad base-angle distribution of real-random pyramids yields superior scattering performance. In particular, an ergodic distribution of light rays within the wafer—typical of Lambertian scatterers—is reached after fewer bounces than in the ideal-random pyramids case: two passes through the wafer vs four. Similarly, the escape reflection is lower with real-random pyramids and is in fact lower even than the Lambertian case after five passes through the wafer. Finally, we showed that the total path-length enhancement provided by real-random pyramid textures exceeds the $4n^2$ Lambertian case for a restricted range of incident angles, counterbalanced by sub-Lambertian performance at higher angles. Hence, real-random pyramid textures exhibit an angle-selective behavior, which does not violate the physics of light trapping. Perhaps most important, ideal-random pyramids with 54.7° base angles offer a poor approximation of the behavior of actual textured wafers. A simple Lambertian assumption is a better approximation, particularly if coupled with an exceptional (non-Lambertian) first pass in which all light is assumed to travel toward the rear of the wafer at 36.5° with respect to the wafer normal.

The framework we presented in this contribution can be applied to other surface textures, including mathematically generated artificial textures, provided that the size of features does not preclude the use of geometric optics. Similarly, parasitic absorption and imperfect antireflection coatings can be incorporated into the optical simulations to treat particular cases of interest. Angular distribution functions are a powerful tool to investigate the evolution of light within a substrate, as they provide insight into the underlying mechanism(s) responsible for lumped behavior, such as poor photocurrent within a textured solar cell. Small variations in the features of actual textures, relative to the intended design texture, may appear insignificant in a topographical map, but their pronounced effect on the evolution of trapped light becomes apparent in simulated angular distribution functions.

ACKNOWLEDGMENTS

This material is based upon work supported primarily by USAID through the U.S.-Pakistan Center for Advanced Studies in Energy program, under Award No. AID-391-A-15-00001 and through the Engineering Research Center Program of the National Science Foundation and the Office of Energy Efficiency and Renewable Energy of the Department of Energy under NSF Cooperative Agreement No. EEC-1041895.

APPENDIX A: LOCAL ADF AFTER REFLECTION AT THE TOP SURFACE

Figure 10, which is complementary to Fig. 7, shows L-ADFs of light rays after reflection off the front or rear pyramid facets.

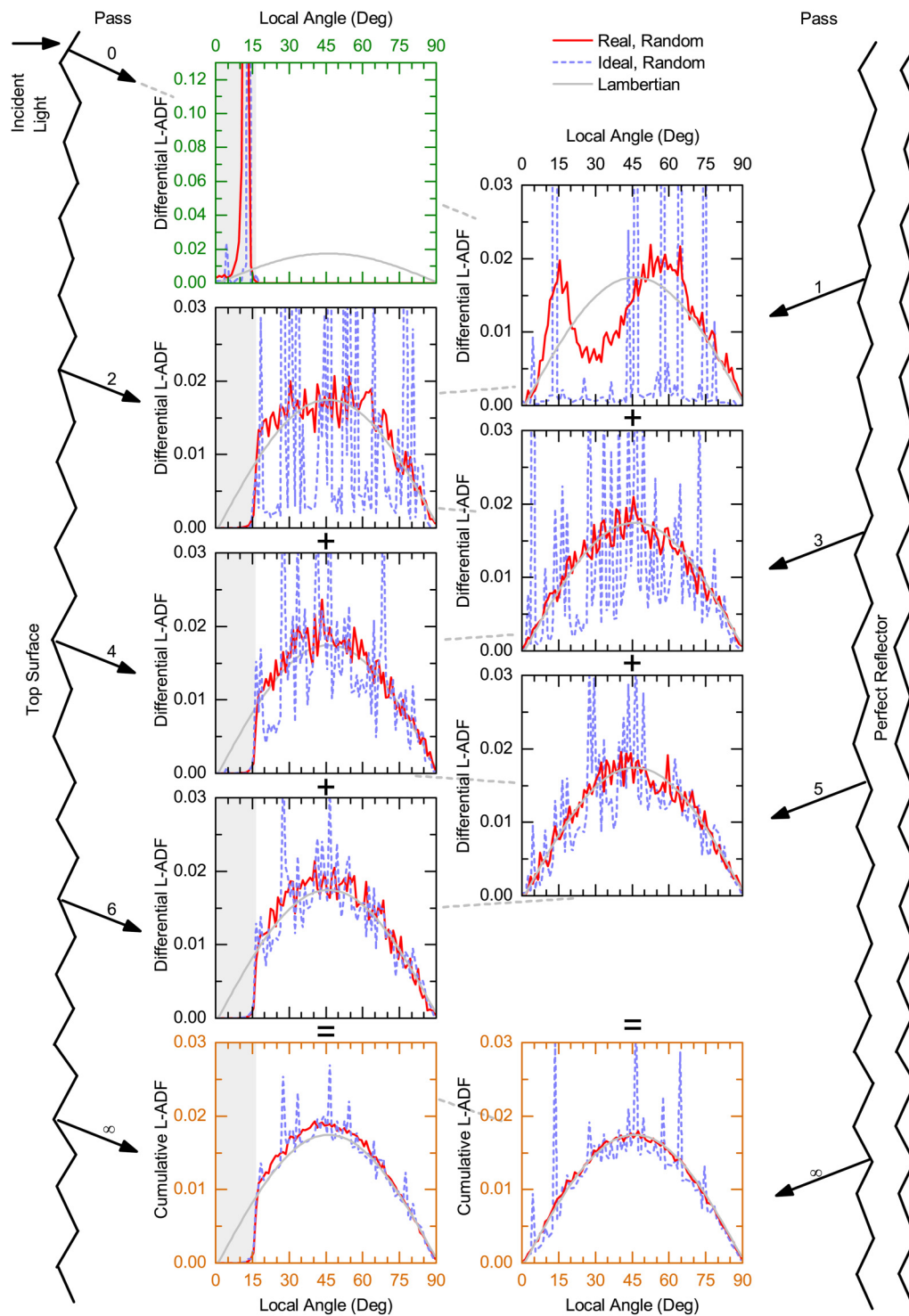


FIG. 10. Evolution of the local angle distribution function (L-ADF) as normally incident light rays that are trapped in the wafer makes multiple passes between the front and rear surfaces. This figure is the same as Fig. 7 with only one exception: the L-ADFs reported at the top surface is *after* the light rays have hit the top surface. Therefore, the light rays that fell into the escape cone, which spans between 0° to 16° , has escaped from the wafer.